Three-dimensional Modeling, Simulation and Capacity Analysis of Space-time Correlated Mobile-to-mobile Channels

Alenka G. Zajić, *Student Member, IEEE,* and Gordon L. Stüber, *Fellow, IEEE*

***Abstract*— A three-dimensional (3-D) reference model is proposed for multiple-input multiple-output (MIMO) mobile-to-mobile (M-to-M) multipath-fading channels. From this model, a closed-form joint space-time correlation function is derived for a 3-D non-isotropic scattering environment. Two sum-of-sinusoids based 3-D simulation models for MIMO M-to-M multipath-fading channels are proposed. The statistics of the simulation models are verified by simulation. Finally, these simulation models are used to evaluate the effect of the space-time correlation on the outage capacity of uniform linear antenna arrays and to compare the capacities of linear, circular, and spherical antenna arrays.**

***Index Terms*— Mobile-to-mobile channels, three-dimensional scattering environment, sum-of-sinusoids based channel simulators, antenna arrays, capacity analysis.**

I. Introduction

MOBILE-to-mobile (M-to-M) communications play an important role in mobile ad-hoc wireless networks, intelligent transportation systems, and relay-based cellular networks. M-to-M communication systems are equipped with low elevation antennas with both the transmitter ($\mathrm{T_x}$) and receiver ($\mathrm{R_x}$) in motion. To successfully design M-to-M systems, a detailed knowledge of the multipath fading channel and its statistical properties is required. Early studies of single-input single-output (SISO) M-to-M fading channels have been reported by Akki and Haber [1], [2]. They proposed a mathematical reference model and showed that the received envelope of SISO M-to-M channels is Rayleigh faded under non-line-of-sight conditions, but the statistical properties differ from cellular fixed-to-mobile (F-to-M) channels with elevated base station antennas that are free of local scattering. Simulation models for SISO M-to-M channels have been reported in [3]-[5]. Channel measurements for SISO narrowband mobile-to-mobile communications have been reported in [6]. Recently, using the "two-ring" geometrical model in [7], the reference models for narrowband multiple-input multiple-output (MIMO) M-to-M channels have been proposed in [8], [9]. The simulation models for narrowband MIMO M-to-M channels have been provided in [10], [11].

All previously reported models assume that the fields incident on the $\mathrm{T_x}$ or $\mathrm{R_x}$ antennas are composed of a number of waves travelling only in the *horizontal* plane. This assumption is valid only for certain environments, e.g., rural areas. However, it seems inappropriate for urban environments where the $\mathrm{T_x}$ and $\mathrm{R_x}$ antenna arrays are often located in close proximity to and lower than the surrounding buildings. Scattered waves may propagate by diffraction from the edges of buildings down to the street and, thus, not necessarily travel horizontally. In contrast, this paper proposes a three-dimensional (3-D) reference model for MIMO M-to-M multipath fading channels. First, we introduce a *two-cylinder* 3-D geometrical propagation model for MIMO M-to-M channels that includes elevation components into our two-dimensional (2-D) model proposed in [9]. The two-cylinder model can be considered as an extension of the one-cylinder model for cellular F-to-M channels proposed in [12], [13]. By taking into account local scattering around both the $\mathrm{T_x}$ and $\mathrm{R_x}$, and by including mobility of both the $\mathrm{T_x}$ and $\mathrm{R_x}$, we obtain our two-cylinder model. Then, by using this model, we propose a new 3-D reference model. From the 3-D reference model, we derive a closed-form joint space-time correlation function for a 3-D non-isotropic scattering environment. Several existing 2-D M-to-M, 2-D F-to-M and 3-D F-to-M correlation functions are shown to be special cases of our 3-D MIMO M-to-M space-time correlation function. However, as shown later, not all of 2-D and 3-D F-to-M correlation functions can be obtained from our 3-D MIMO M-to-M space-time correlation function.

The reference model assumes an infinite number of scatterers, which prevents practical implementation. Hence, we propose deterministic and statistical sum-of-sinusoids (SoS) based simulation models for a 3-D non-isotropic scattering environment. The statistical properties of our models are verified by simulations. We use our statistical simulation model to evaluate the effect of the space-time correlation on the outage capacity of uniform linear antenna arrays (ULAs) and to compare the capacities of linear, circular, and spherical antenna arrays. First, we study the effect of antenna spacing on the outage capacity. Our results show that increasing the distances between ULA elements beyond 2λ has a negligible effect on the outage capacity. These results differ from the results

Paper approved by Dr. Kapil Dandekar, the Associate Editor for IEEE Transactions on Vehicular Technology. Manuscript received September 21, 2006; revised April 3, 2007, May 30, 2007, August 6, 2007, and September 14, 2007. This work was prepared through collaborative participation in the Collaborative Technology Alliance for Communications & Networks sponsored by the U.S. Army Research Laboratory under Cooperative Agreement DAAD19-01-2-0011. The U.S. Government is authorized to reproduce and distribute reprints for Government purposes notwithstanding any copyright notation thereon. The views and conclusions contained in this document are those of the authors and should not be interpreted as representing the official policies, either expressed or implied, of the Army Research Laboratory or the U. S. Government.

Alenka G. Zajić and Gordon L. Stüber are with the School of Electrical and Computer Engineering, Georgia Inst. of Tech., Atlanta, GA 30332 USA.

obtained for cellular F-to-M channels (with fixed, elevated base station antennas), where increasing $\mathrm{R_x}$ antenna element spacing beyond 5λ and $\mathrm{T_x}$ antenna element spacing beyond 2λ has a negligible effect on the capacity [7]. Second, we study the effect of antenna orientation angles on the outage capacity. When the radio propagation environment is characterized by 2-D *isotropic* scattering, the orientations of the $\mathrm{T_x}$ and $\mathrm{R_x}$ antenna arrays in the x - y plane are observed to have no influence on the capacity. This property of M-to-M channels is in contrast to cellular F-to-M channels, where the $\mathrm{T_x}$ broadside antenna arrays (array elements placed on the y - axis) and $\mathrm{R_x}$ inline antenna arrays (array elements placed on the x - axis) provide higher capacity than the $\mathrm{T_x}$ and $\mathrm{R_x}$ broadside antenna arrays [14], [15]. When the radio propagation environment is characterized by 2-D *non-isotropic* scattering, the optimum capacity depends on the relative angle between the $\mathrm{T_x}$ ($\mathrm{R_x}$) antenna array and the orientation of local scatterers around the $\mathrm{T_x}$ ($\mathrm{R_x}$). Furthermore, our results show that if the available area in the x - y plane is insufficient for the antenna array realization, the antenna array can be vertically tilted without a significant capacity loss. The results also show that the 2-D models actually underestimate available capacity. Finally, we compare the capacities of linear, circular, and spherical antenna arrays. The results show that if volume available for antenna array realization is constrained, circular antenna arrays placed in the x - y plane will provide the highest capacity.

The remainder of this paper is organized as follows. Section II describes the system geometry and presents the 3-D reference model for MIMO M-to-M channels. Section III presents the derivation of the closed-form joint space-time correlation function for 3-D non-isotropic scattering. Section IV presents the 3-D SoS deterministic and statistical simulation models. Section V briefly reviews MIMO channel capacity, evaluates the effect of the space-time correlation on the outage capacity of ULAs, and compares the capacities of uniform linear, circular, and spherical antenna arrays. Finally, Section VI provides some concluding remarks.

II. A 3-D Reference Model for MIMO Mobile-to-Mobile Channels

This paper considers a narrowband MIMO communication system with L_T transmit and L_R receive omnidirectional antenna elements. Both the transmitter ($\mathrm{T_x}$) and receiver ($\mathrm{R_x}$) are in motion and are equipped with low elevation antennas. The radio propagation environment is characterized by 3-D scattering with non-line-of-sight (NLoS) propagation conditions between the $\mathrm{T_x}$ and $\mathrm{R_x}$. The MIMO channel is described by an $L_R \times L_T$ matrix $\mathbf{H}(t) = [h_{ij}(t)]_{L_R \times L_T}$ of complex low-pass faded envelopes.

Fig. 1 shows our two-cylinder model for a MIMO M-to-M channel with $L_T = L_R = 2$ antenna elements. This elementary 2×2 antenna configuration will be used later to construct linear, circular, and spherical multielement antenna arrays. The two-cylinder model defines two cylinders, one around the $\mathrm{T_x}$ and another around the $\mathrm{R_x}$, as shown in Fig. 1. Around the transmitter, M fixed omnidirectional scatterers lie on the surface of a cylinder of radius R_t, and the m^{th} transmit scatterer is denoted by $S_T^{(m)}$. Similarly, around the receiver, N fixed omnidirectional scatterers lie on the surface of a cylinder with radius R_r, and the n^{th} receive scatterer is denoted by $S_R^{(n)}$. The parameters in Fig. 1 are defined in Table I.

It is assumed that the radii R_t and R_r are much smaller than the distance D, i.e., $\max\{R_t, R_r\} \ll D$ (local scattering condition). Furthermore, it is assumed that the distance D is smaller than $4R_tR_rL_R/(\lambda(L_T-1)(L_R-1))$ (channel does not experience keyhole behavior [16]), where λ denotes the carrier wavelength. Finally, it is assumed that the spacing between two antenna elements at $\mathrm{T_x}$ and $\mathrm{R_x}$, $d_T(p,\tilde{p})$ and $d_R(q,\tilde{q})$, are much smaller than the radii R_t and R_r, i.e., $\max\{d_T(p,\tilde{p}), d_R(q,\tilde{q})\} \ll \min\{R_t, R_r\}$.

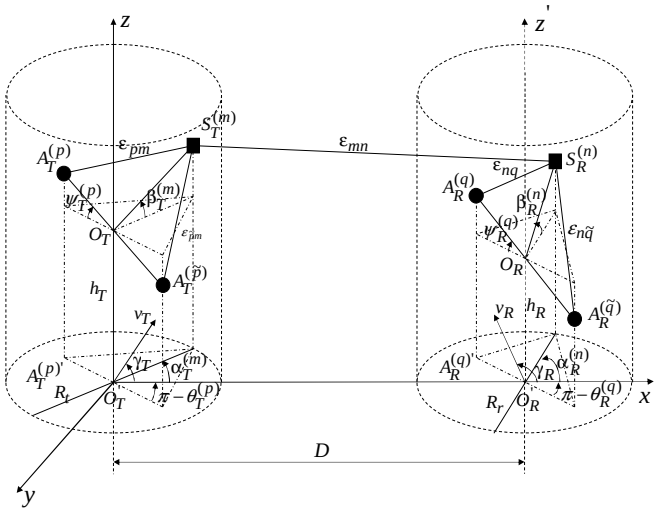

Fig. 1. The 3-D geometrical model for MIMO M-to-M channels with $L_T = L_R = 2$ antenna elements.

Observing Fig. 1 and using results in [7], [8], the distances ϵ_{pm}, $\epsilon_{\tilde{p}m}$, ϵ_{mn}, $\epsilon_{n\tilde{q}}$, and ϵ_{nq} can be expressed as functions of the random angles $\alpha_T^{(m)}$, $\alpha_R^{(n)}$, $\beta_T^{(m)}$, and $\beta_R^{(n)}$ as follows:

$$\begin{aligned}\epsilon_{p/\tilde{p},m} \approx\ & \frac{R_t}{\cos\beta_T^{(m)}} - d(A_T^{(p/\tilde{p})}, O_T)\sin\psi_T^{(p/\tilde{p})}\sin\beta_T^{(m)} \\ & - d(A_T^{(p/\tilde{p})}, O_T)\cos\theta_T^{(p/\tilde{p})}\cos\psi_T^{(p/\tilde{p})}\cos\alpha_T^{(m)}\cos\beta_T^{(m)} \\ & - d(A_T^{(p/\tilde{p})}, O_T)\sin\theta_T^{(p/\tilde{p})}\cos\psi_T^{(p/\tilde{p})}\sin\alpha_T^{(m)}\cos\beta_T^{(m)}, \quad (1)\end{aligned}$$

$$\begin{aligned}\epsilon_{n,q/\tilde{q}} \approx\ & \frac{R_r}{\cos\beta_R^{(n)}} - d(A_R^{(q/\tilde{q})}, O_R)\sin\psi_R^{(q/\tilde{q})}\sin\beta_R^{(n)} \\ & - d(A_R^{(q/\tilde{q})}, O_R)\cos\theta_R^{(q/\tilde{q})}\cos\psi_R^{(q/\tilde{q})}\cos\alpha_R^{(n)}\cos\beta_R^{(n)} \\ & - d(A_R^{(q/\tilde{q})}, O_R)\sin\theta_R^{(q/\tilde{q})}\cos\psi_R^{(q/\tilde{q})}\sin\alpha_R^{(n)}\cos\beta_R^{(n)}, \quad (2)\end{aligned}$$

$$\epsilon_{mn} \approx \sqrt{D^2 + (h_T - h_R)^2} \approx D, \quad (3)$$

where $p \in \{1,\ldots,L_T\}$, $q \in \{1,\ldots,L_R\}$, and parameters $d(A_T^{(p/\tilde{p})}, O_T)$ and $d(A_R^{(q/\tilde{q})}, O_R)$ denote distances (positive scalars) between the p^{th} transmit antenna element and the center of the $\mathrm{T_x}$ antenna array and the q^{th} receive antenna element and the center of the $\mathrm{R_x}$ antenna array, respectively.

From the 3-D geometrical model, we observe that the waves from the $\mathrm{T_x}$ antenna elements impinge on the scatterers

TABLE I
DEFINITION OF PARAMETERS IN FIGURE 1.

D	The distance between the centers of the Tx and Rx cylinders.
R_t, R_r	The radius of the Tx and Rx cylinder, respectively.
$d_T(p,\tilde{p})$	The spacing between p^{th} and $\tilde{p}^{th}$ antenna elements at the Tx.
$d_R(q,\tilde{q})$	The spacing between q^{th} and $\tilde{q}^{th}$ antenna elements at the Rx.
$\theta_T^{(p)}$, $\theta_R^{(q)}$	The azimuth angle of the p^{th} transmit and q^{th} receive antenna element (relative to the *x*-axis), respectively.
$\psi_T^{(p)}$, $\psi_R^{(q)}$	The elevation angle of the p^{th} transmit and q^{th} receive antenna element (relative to the *x*-*y* plane), respectively.
v_T, v_R	The velocities of the Tx and Rx, respectively.
γ_T, γ_R	The moving directions of the Tx and Rx, respectively.
$\alpha_T^{(m)}$,$\alpha_R^{(n)}$	The azimuth angles of departure (AAoD) and the azimuth angles of arrival (AAoA), respectively.
$\beta_T^{(m)}$,$\beta_R^{(n)}$	The elevation angles of departure (EAoD) and the elevation angles of arrival (EAoA), respectively.
ε_{pm}, $\varepsilon_{\tilde{p}m}$, ε_{mn}, ε_{nq}, and $\varepsilon_{n\tilde{q}}$	The distances $d\left(A_T^{(p)},S_T^{(m)}\right)$, $d\left(A_T^{(\tilde{p})},S_T^{(m)}\right)$, $d\left(S_T^{(m)},S_R^{(n)}\right)$, $d\left(S_R^{(n)},A_R^{(q)}\right)$, and $d\left(S_R^{(n)},A_R^{(\tilde{q})}\right)$
h_T, h_R	The distances $d\left(O_T,O_T^{'}\right)$ and $d\left(O_R,O_R^{'}\right)$, respectively.

located on the $\mathrm{T_x}$ cylinder and scatter from the scatterers located on the $\mathrm{R_x}$ cylinder before they arrive at the $\mathrm{R_x}$ antenna elements. In contrast to NLoS cellular F-to-M channels where single-bounced waves are prevalent, in NLoS urban M-to-M channels the double-bounced waves are dominant. In the 3-D reference model, the number of local scatterers around the $\mathrm{T_x}$ and $\mathrm{R_x}$ is infinite. Consequently, the received complex faded envelope of the link $A_T^{(p)} - A_R^{(q)}$ is

$$h_{pq}(t) = \lim_{M,N\to\infty} \sqrt{\frac{1}{MN}} \sum_{m=1}^{M}\sum_{n=1}^{N} G_p\left(\alpha_T^{(m)},\beta_T^{(m)}\right) G_q\left(\alpha_R^{(n)},\beta_R^{(n)}\right) \times e^{-j\frac{2\pi}{\lambda}(\epsilon_{pm}+\epsilon_{mn}+\epsilon_{nq})+j\phi_{mn}+j2\pi t f_{T\max}\cos(\alpha_T^{(m)}-\gamma_T)\cos\beta_T^{(m)}} \times e^{j2\pi t f_{R\max}\cos(\alpha_R^{(n)}-\gamma_R)\cos\beta_R^{(n)}}, \quad (4)$$

where $f_{T\max} = v_T/\lambda$ and $f_{R\max} = v_R/\lambda$ are the maximum Doppler frequencies associated with the $\mathrm{T_x}$ and $\mathrm{R_x}$, respectively, and $G_p(\alpha_T^{(m)},\beta_T^{(m)})$ and $G_q(\alpha_R^{(n)},\beta_R^{(n)})$ denote the antenna patterns of the p^{th} transmit and q^{th} receive antenna element, respectively. Since omnidirectional antenna elements are assumed (i.e., antenna patterns can be normalized to one), the antenna patterns are omitted in further analysis. It is assumed that the azimuth and elevation angles of departure (AAoDs and EAoDs) and the azimuth and elevation angles of arrival (AAoAs and EAoAs) are random variables. Since all rays are double-bounced, the angles of departure are independent from the angles of arrival [16]. Finally, it is assumed that the phases ϕ_{mn} are random variables uniformly distributed on the interval $[-\pi,\pi)$ and independent from the angles of departure and angles of arrival.

Using (1) - (3), the complex faded envelope in (4) can be rewritten as

$$h_{pq}(t) = \lim_{M,N\to\infty} \frac{1}{\sqrt{MN}} \sum_{m=1}^{M}\sum_{n=1}^{N} a_{p,m}\ b_{n,q}\ e^{j\phi_{mn}} \times e^{j2\pi t[f_{T\max}\cos(\alpha_T^{(m)}-\gamma_T)\cos\beta_T^{(m)}+f_{R\max}\cos(\alpha_R^{(n)}-\gamma_R)\cos\beta_R^{(n)}]}, \quad (5)$$

where

$$a_{p,m} = e^{-j\frac{\pi}{\lambda}D-j\frac{2\pi}{\lambda}R_t/\cos\beta_T^{(m)}+j\frac{2\pi}{\lambda}d_{T_x}^{(p)}\cos\alpha_T^{(m)}\cos\beta_T^{(m)}} \times e^{j\frac{2\pi}{\lambda}d_{T_y}^{(p)}\sin\alpha_T^{(m)}\cos\beta_T^{(m)}+j\frac{2\pi}{\lambda}d_{T_z}^{(p)}\sin\beta_T^{(m)}} \quad (6)$$

$$b_{n,q} = e^{-j\frac{\pi}{\lambda}D-j\frac{2\pi}{\lambda}R_r/\cos\beta_R^{(n)}+j\frac{2\pi}{\lambda}d_{R_x}^{(q)}\cos\alpha_R^{(n)}\cos\beta_R^{(q)}} \times e^{j\frac{2\pi}{\lambda}d_{R_y}^{(q)}\sin\alpha_R^{(n)}\cos\beta_R^{(n)}+j\frac{2\pi}{\lambda}d_{R_z}^{(q)}\sin\beta_R^{(n)}}, \quad (7)$$

$$d_{T_x}^{(p)} = d(A_T^{(p)},O_T)\cos\theta_T^{(p)}\cos\psi_T^{(p)}, \quad (8)$$

$$d_{T_y}^{(p)} = d(A_T^{(p)},O_T)\sin\theta_T^{(p)}\cos\psi_T^{(p)}, \quad (9)$$

$$d_{T_z}^{(p)} = d(A_T^{(p)},O_T)\sin\psi_T^{(p)}, \quad (10)$$

$$d_{R_x}^{(q)} = d(A_R^{(q)},O_R)\cos\theta_R^{(q)}\cos\psi_R^{(q)}, \quad (11)$$

$$d_{R_y}^{(q)} = d(A_R^{(q)},O_R)\sin\theta_R^{(q)}\cos\psi_R^{(q)}, \quad (12)$$

$$d_{R_z}^{(q)} = d(A_R^{(q)},O_R)\sin\psi_R^{(q)}. \quad (13)$$

Parameters $d_{T_x}^{(p)}$, $d_{T_y}^{(p)}$, and $d_{T_z}^{(p)}$ are coordinates of the p^{th} transmit antenna element relative to the center of $\mathrm{T_x}$ antenna array, whereas parameters $d_{R_x}^{(q)}$, $d_{R_y}^{(q)}$, and $d_{R_z}^{(q)}$ are coordinates of the q^{th} receive antenna element relative to the center of $\mathrm{R_x}$ antenna array. Note that these parameters depend on antenna array configuration and can be positive or negative numbers. In this paper, we focus on the uniform linear antenna arrays(ULA), the uniform circular antenna arrays (UCA), and the spherical antenna arrays. For ULAs, the coordinates of antenna elements are defined as follows:

$$d_{T_x/R_x}^{(p/q)} = \frac{1}{2}(L_{T/R}+1-2p(q))d_{T/R}\cos\theta_{T/R}\cos\psi_{T/R}, \quad (14)$$

$$d_{T_y/R_y}^{(p/q)} = \frac{1}{2}(L_{T/R}+1-2p(q))d_{T/R}\sin\theta_{T/R}\cos\psi_{T/R}, \quad (15)$$

$$d_{T_z/R_z}^{(p/q)} = \frac{1}{2}(L_{T/R}+1-2p(q))d_{T/R}\sin\psi_{T/R}, \quad (16)$$

where $d_{T/R}$ denotes the spacing between two adjacent antenna elements at the transmitter/receiver, $\theta_{T/R}$ describes the orientation of all transmit/receive antenna elements in the x - y plane (relative to the x - axis), and $\psi_{T/R}$ describes the elevation angle of all transmit/receive antenna elements, relative to the x - y plane. For UCAs, the coordinates of antenna elements are defined as follows:

$$d_{T_x/R_x}^{(p/q)} = r_{T/R}\cos\left(\frac{2\pi p(q)}{L_{T/R}}\right)\cos\psi_{T/R}, \quad (17)$$

$$d_{T_y/R_y}^{(p/q)} = r_{T/R}\sin\left(\frac{2\pi p(q)}{L_{T/R}}\right)\cos\psi_{T/R}, \quad (18)$$

$$d_{T_z/R_z}^{(p/q)} = r_{T/R}\sin\psi_{T/R}, \quad (19)$$

where $r_{T/R}$ denotes the radius of the transmit/receive antenna array circle and $\psi_{T/R}$ describes the elevation angle of all transmit/receive antenna elements, relative to the x - y plane. Finally, for spherical antenna arrays, the coordinates of antenna elements are defined as follows:

$$d_{T_x/R_x}^{(p/q)} = r_{T/R}\cos\theta_{T/R}^{(p/q)}\cos\psi_{T/R}^{(p/q)}, \quad (20)$$

$$d_{T_y/R_y}^{(p/q)} = r_{T/R}\sin\theta_{T/R}^{(p/q)}\cos\psi_{T/R}^{(p/q)}, \quad (21)$$

$$d_{T_z/R_z}^{(p/q)} = r_{T/R}\sin\psi_{T/R}^{(p/q)}, \quad (22)$$

where $r_{T/R}$ denotes the radius of the transmit/receive spherical antenna array, $\theta_{T/R}^{(p/q)}$ denotes the azimuth angle of the p^{th} transmit (q^{th} receive) antenna element relative to the x - axis, and $\psi_{T/R}^{(p/q)}$ denotes the elevation angle of the p^{th} transmit (q^{th} receive) antenna element relative to the x - y plane.

III. Space-Time Correlation Function of the 3-D Reference Model

Assuming a 3-D non-isotropic scattering environment, we now derive the space-time correlation function of the complex faded envelope described in (5). The normalized space-time correlation function between two complex faded envelopes $h_{pq}(t)$ and $h_{\tilde{p}\tilde{q}}(t)$ is defined as

$$R_{pq,\tilde{p}\tilde{q}}[\tau] = \frac{\mathrm{E}\left[h_{pq}(t)h_{\tilde{p}\tilde{q}}^{*}(t+\tau)\right]}{\sqrt{\mathrm{E}[|h_{pq}(t)|^2]\mathrm{E}[|h_{\tilde{p}\tilde{q}}(t)|^2]}}, \quad (23)$$

where $(\ \cdot\ )^*$ denotes the complex conjugate operation, $\mathrm{E}[\ \cdot\ ]$ is the statistical expectation operator, $p,\tilde{p} \in \{1,\ldots,L_T\}$, and $q,\tilde{q} \in \{1,\ldots,L_R\}$. Using (5) and (23), the space-time correlation function can be written as

$$R_{pq,\tilde{p}\tilde{q}}[\tau] = \lim_{M,N\to\infty}\frac{1}{MN}\sum_{m=1}^{M}\sum_{n=1}^{N}\mathrm{E}\Big[a_{p,m}\ b_{n,q}\ a_{\tilde{p},m}^{*}\ b_{n,\tilde{q}}^{*} \quad (24)$$
$$e^{-j2\pi\tau\left[f_{T\max}\cos(\alpha_T^{(m)}-\gamma_T)\cos\beta_T^{(m)}+f_{R\max}\cos(\alpha_R^{(n)}-\gamma_R)\cos\beta_R^{(n)}\right]}\Big].$$

Since the number of local scatterers in the reference model described in Section II is infinite, the discrete AAoDs, $\alpha_T^{(m)}$, EAoDs, $\beta_T^{(m)}$, AAoAs, $\alpha_R^{(n)}$, and EAoAs, $\beta_R^{(n)}$, can be replaced with continuous random variables α_T, β_T, α_R, and β_R with joint probability density functions (pdfs) $f(\alpha_T,\beta_T)$ and $f(\alpha_R,\beta_R)$, respectively. We assume that the azimuth and elevation angles are independent of each other, and thus, the joint pdfs $f(\alpha_T,\beta_T)$ and $f(\alpha_R,\beta_R)$ can be decomposed to $f(\alpha_T)f(\beta_T)$ and $f(\alpha_R)f(\beta_R)$, respectively. This assumption is based on experimental data in [17], [18]. Hence, (24) can be rewritten as

$$R_{pq,\tilde{p}\tilde{q}}[\tau] = \int_{-\beta_{R_m}}^{\beta_{R_m}}\int_{-\beta_{T_m}}^{\beta_{T_m}}\int_{-\pi}^{\pi}\int_{-\pi}^{\pi} e^{-j2\pi\tau f_{T\max}\cos(\alpha_T-\gamma_T)\cos\beta_T} \quad (25)$$
$$\times\, e^{-j2\pi\tau f_{R\max}\cos(\alpha_R-\gamma_R)\cos\beta_R + j\frac{2\pi}{\lambda}\left[d_{T_x}^{(p,\tilde{p})}\cos\alpha_T\cos\beta_T + d_{T_z}^{(p,\tilde{p})}\sin\beta_T\right]}$$
$$\times\, e^{j\frac{2\pi}{\lambda}\left[d_{T_y}^{(p,\tilde{p})}\sin\alpha_T\cos\beta_T + d_{R_x}^{(q,\tilde{q})}\cos\alpha_R\cos\beta_R + d_{R_y}^{(q,\tilde{q})}\sin\alpha_R\cos\beta_R\right]}$$
$$\times\, e^{j\frac{2\pi}{\lambda}\left[d_{R_z}^{(q,\tilde{q})}\sin\beta_R\right]} f(\alpha_T)f(\beta_T)f(\alpha_R)f(\beta_R)d\alpha_T d\beta_T d\alpha_R d\beta_R,$$

where $d_{T_x}^{(p,\tilde{p})} = d_{T_x}^{(p)} - d_{T_x}^{(\tilde{p})}$, $d_{T_y}^{(p,\tilde{p})} = d_{T_y}^{(p)} - d_{T_y}^{(\tilde{p})}$, $d_{T_z}^{(p,\tilde{p})} = d_{T_z}^{(p)} - d_{T_z}^{(\tilde{p})}$, $d_{R_x}^{(q,\tilde{q})} = d_{R_x}^{(q)} - d_{R_x}^{(\tilde{q})}$, $d_{R_y}^{(q,\tilde{q})} = d_{R_y}^{(q)} - d_{R_y}^{(\tilde{q})}$, $d_{R_z}^{(q,\tilde{q})} = d_{R_z}^{(q)} - d_{R_z}^{(\tilde{q})}$, and β_{T_m} and β_{R_m} are the non-negative maximum elevation angles of the scatterers around the $\mathrm{T_x}$ and $\mathrm{R_x}$, respectively.

Several different scatterer distributions, such as uniform [19], von Mises [20], Gaussian, and Laplacian [21], are used in prior work to characterize the random azimuth angles α_T and α_R. In this paper, we use the von Mises pdf because it approximates many of the previously mentioned distributions and leads to closed-form solutions for many useful situations. The von Mises pdf is defined as [20]

$$f(\theta) = \frac{1}{2\pi I_0(k)}\exp\left[k\cos(\theta-\mu)\right], \quad (26)$$

where $\theta \in [-\pi,\pi)$, $I_0(\ \cdot\ )$ is the zeroth-order modified Bessel function of the first kind, $\mu \in [-\pi,\pi)$ is the mean angle at which the scatterers are distributed in the x - y plane, and k controls the spread of scatterers around the mean. Prior work uses several different scatterer distributions, such as uniform [22], cosine [13], and Gaussian [23], to characterize the random elevation angles β_T and β_R. Here, we use the pdf [13]

$$f(\varphi) = \begin{cases} \frac{\pi}{4\varphi_m}\cos\left(\frac{\pi}{2}\frac{\varphi}{\varphi_m}\right) & ,\ |\varphi| \le \varphi_m \le \frac{\pi}{2} \\ 0 & ,\ \text{otherwise} \end{cases} \quad (27)$$

because it matches well the experimental data in [18]. Parameter φ_m is the absolute value of the maximum elevation angle and lies in the range $0^\circ \le \varphi_m \le 20^\circ$ [18]. Such elevation angles are typical for the "street-canyon" type of propagation [24], which is prevalent in mobile-to-mobile communications where both the $\mathrm{T_x}$ and $\mathrm{R_x}$ are in motion and equipped with low elevation antennas (e.g., two cars driving through streets). Note that elevation angles between 20° and 80° have been observed for "over the roof" propagation [24], which is characteristic for fixed-to-mobile communications where the base-station is elevated above the roofs of the buildings.

By grouping the terms in (25) into those containing α_T and β_T and those containing α_R and β_R, the integrals in (25) reduce to the product of two double integrals, because the random angles α_T and β_T are independent from the random angles α_R and β_R. By denoting the von Mises pdf for the $\mathrm{T_x}$ and $\mathrm{R_x}$ azimuth angles as $f(\alpha_T) = \exp\left[k_T\cos(\alpha_T-\mu_T)\right]/(2\pi I_0(k_T))$ and $f(\alpha_R) = \exp\left[k_R\cos(\alpha_R-\mu_R)\right]/(2\pi I_0(k_R))$, respectively, and by denoting the pdf for the $\mathrm{T_x}$ and $\mathrm{R_x}$ elevation angles as $f(\beta_T) = \pi\cos(\pi\beta_T/(2\beta_{T_m}))/(4\beta_{T_m})$ and $f(\beta_R) = \pi\cos(\pi\beta_R/(2\beta_{R_m}))/(4\beta_{R_m})$, respectively, using trigonometric transformations, and the equality $\int_{-\pi}^{\pi}\exp\{a\sin(c) + b\cos(c)\}dc = 2\pi I_0(\sqrt{a^2+b^2})$ [25, eq. 3.338-4], the space-time correlation function becomes

$$R_{pq,\tilde{p}\tilde{q}}[\tau] = \int_{-\beta_{T_m}}^{\beta_{T_m}}\cos\left(\frac{\pi}{2}\frac{\beta_T}{\beta_{T_m}}\right)\frac{\pi e^{j\frac{2\pi}{\lambda}d_{T_z}^{(p,\tilde{p})}\sin\beta_T}}{4\beta_{T_m}}$$
$$\times\ \frac{I_0\left(\sqrt{x^2+y^2}\cos\beta_T\right)}{I_0(k_T)}d\beta_T\int_{-\beta_{R_m}}^{\beta_{R_m}}\cos\left(\frac{\pi}{2}\frac{\beta_R}{\beta_{R_m}}\right)$$
$$\times\ \frac{\pi e^{j\frac{2\pi}{\lambda}d_{R_z}^{(q,\tilde{q})}\sin\beta_R}}{4\beta_{R_m}}\frac{I_0\left(\sqrt{z^2+w^2}\cos\beta_R\right)}{I_0(k_R)}d\beta_R, \quad (28)$$

where parameters x, y, z, and w are defined as $x = j2\pi d_{T_x}^{(p,\tilde{p})}/\lambda - j2\pi\tau f_{T\max}\cos\gamma_T + k_T\cos\mu_T/\cos\beta_T$, $y = j2\pi d_{T_y}^{(p,\tilde{p})}/\lambda - j2\pi\tau f_{T\max}\sin\gamma_T + k_T\sin\mu_T/\cos\beta_T$, $z = j2\pi d_{R_x}^{(q,\tilde{q})}/\lambda - j2\pi\tau f_{R\max}\cos\gamma_R + k_R\cos\mu_R/\cos\beta_R$, $w =$

$j2\pi d_{R_y}^{(q,\tilde{q})}/\lambda - j2\pi\tau f_{R\max}\sin\gamma_R + k_R \sin\mu_R/\cos\beta_R$. To obtain the space-time correlation function for 3-D MIMO M-to-M channels, the integrals in (28) must be evaluated numerically, because they lack closed-form solutions. However, since β_T and β_R are small angles, i.e., $\beta_T, \beta_R \leq 20^\circ$, using the small angle approximations $\cos\beta_T, \cos\beta_R \approx 1$, $\sin\beta_T \approx \beta_T$, and $\sin\beta_R \approx \beta_R$, the space-time correlation function can be approximated as

$$\begin{aligned} R_{pq,\tilde{p}\tilde{q}}[\tau] &\approx \frac{I_0\left(\sqrt{x_1^2+y_1^2}\right)}{I_0(k_T)} \frac{I_0\left(\sqrt{z_1^2+w_1^2}\right)}{I_0(k_R)} \\ &\times \int_{-\beta_{T_m}}^{\beta_{T_m}} \frac{\pi}{4\beta_{T_m}} \cos\left(\frac{\pi}{2}\frac{\beta_T}{\beta_{T_m}}\right) e^{j\frac{2\pi}{\lambda}d_{T_z}^{(p,\tilde{p})}\beta_T} d\beta_T \\ &\times \int_{-\beta_{R_m}}^{\beta_{R_m}} \frac{\pi}{4\beta_{R_m}} \cos\left(\frac{\pi}{2}\frac{\beta_R}{\beta_{R_m}}\right) e^{j\frac{2\pi}{\lambda}d_{R_z}^{(q,\tilde{q})}\beta_R} d\beta_R, \end{aligned} \quad (29)$$

where parameters x_1, y_1, z_1, and w_1 are

$$x_1 = j2\pi d_{T_x}^{(p,\tilde{p})}/\lambda - j2\pi\tau f_{T\max}\cos\gamma_T + k_T\cos\mu_T, \quad (30)$$

$$y_1 = j2\pi d_{T_y}^{(p,\tilde{p})}/\lambda - j2\pi\tau f_{T\max}\sin\gamma_T + k_T\sin\mu_T, \quad (31)$$

$$z_1 = j2\pi d_{R_x}^{(q,\tilde{q})}/\lambda - j2\pi\tau f_{R\max}\cos\gamma_R + k_R\cos\mu_R, \quad (32)$$

$$w_1 = j2\pi d_{R_y}^{(q,\tilde{q})}/\lambda - j2\pi\tau f_{R\max}\sin\gamma_R + k_R\sin\mu_R. \quad (33)$$

Finally, solving the integrals in (29), the space-time correlation function becomes

$$\begin{aligned} R_{pq,\tilde{p}\tilde{q}}[\tau] = R_{p,\tilde{p}}^T[\tau] R_{q,\tilde{q}}^R[\tau] &\approx \frac{I_0\left(\sqrt{x_1^2+y_1^2}\right)}{I_0(k_T)} \\ \times \frac{\cos\left(\frac{2\pi}{\lambda}\beta_{T_m} d_{T_z}^{(p,\tilde{p})}\right)}{\left[1-\left(\frac{4\beta_{T_m} d_{T_z}^{(p,\tilde{p})}}{\lambda}\right)^2\right]} & \frac{I_0\left(\sqrt{w_1^2+z_1^2}\right)\cos\left(\frac{2\pi}{\lambda}\beta_{R_m} d_{R_z}^{(q,\tilde{q})}\right)}{I_0(k_R)\left[1-\left(\frac{4\beta_{R_m} d_{R_z}^{(q,\tilde{q})}}{\lambda}\right)^2\right]}. \end{aligned} \quad (34)$$

To illustrate the validity of the approximate space-time correlation function in (34), we compare it with the numerically obtained space-time correlation function in (28). Fig. 2 shows the real and imaginary part of the space-time correlation functions in (28) and (34) obtained assuming a uniform linear array with $L_T = L_R = 2$ antenna elements and the parameters $d_T = d_R = 0.5\lambda$, $\theta_T = \theta_R = \pi/4$, $\psi_T = \psi_R = 2\pi/3$, $\gamma_T = 20^\circ$, $\gamma_R = 40^\circ$, $\mu_T = 70^\circ$, $\mu_R = 20^\circ$, and $k_T = k_R = 20$. Results show excellent agreement between the space-time correlation functions in (28) and (34) for the maximum elevation angles $\beta_{T_m} = \beta_{R_m} = 20^\circ$. The similar results can be obtained for the maximum elevation angles smaller than 20°. Since such elevation angles are typical for M-to-M communications, the space-time correlation function of the M-to-M channel impulse response can be characterized using (34). If "over the roof" propagation occurs, which is characteristic of F-to-M communications, and the maximum elevation angles are larger than 20°, the approximations used to obtain (34) do not hold any more. To illustrate the discrepancy between the exact and approximate space-time correlation functions, Fig. 2 also shows the real and imaginary part of the space-time correlation functions in (28) and (34) obtained for the maximum elevation angles $\beta_{T_m} = \beta_{R_m} = 80^\circ$ (the largest elevation angles found in the literature [24]). The results show that there is still a relatively small discrepancy between the space-time correlation functions in (28) and (34).

Several existing 2-D M-to-M correlation functions are special cases of the 3-D MIMO M-to-M space-time correlation function in (34). The temporal correlation function for SISO M-to-M channels, $J_0(2\pi f_{T\max}\tau)J_0(2\pi f_{R\max}\tau)$ [1] is obtained with $k_T = \beta_{T_m} = 0$ (2-D isotropic scattering around $\mathrm{T_x}$), $k_R = \beta_{R_m} = 0$ (2-D isotropic scattering around $\mathrm{R_x}$), and $d_T = d_R = 0$ (single-antenna $\mathrm{T_x}$ and $\mathrm{R_x}$), where $J_0(\cdot)$ is the zeroth-order Bessel function of the first kind. Similarly, assuming 2-D isotropic scattering, the spatial correlation function for MIMO M-to-M channels $J_0(2\pi d_T/\lambda)J_0(2\pi d_R/\lambda)$ [26], is obtained with $k_T = k_R = 0$, $\beta_{T_m} = \beta_{R_m} = \psi_T = \psi_R = 0$, and $\tau = 0$. Finally, the space-time correlation function for MIMO M-to-M channels, assuming 2-D non-isotropic scattering, $I_0(\sqrt{x^2+y^2})I_0(\sqrt{z^2+w^2})/(I_0(k_T)I_0(k_R))$ [9] is obtained with $\beta_{T_m} = \beta_{R_m} = \psi_T = \psi_R = 0$.

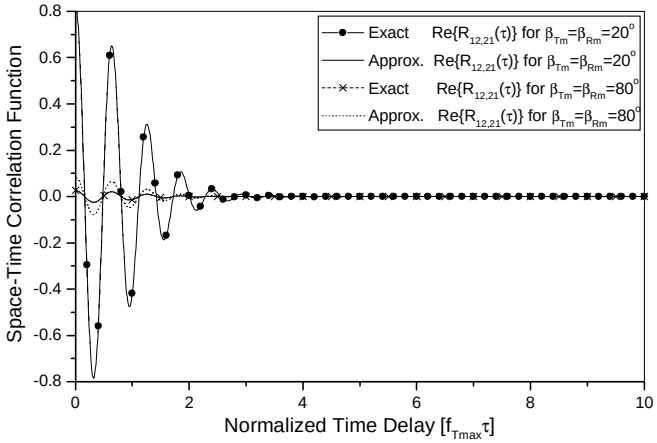

(a)

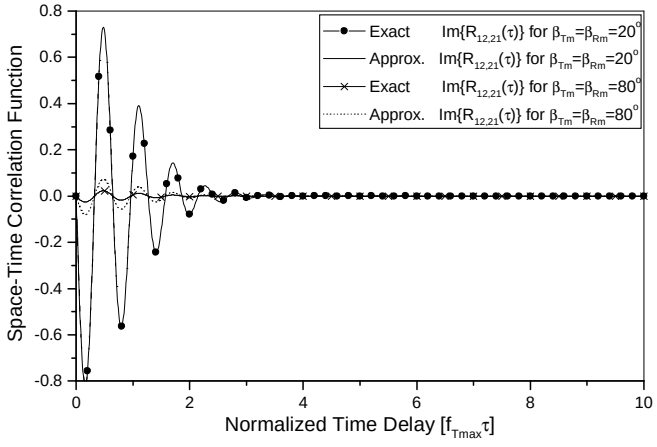

(b)

Fig. 2. The real (a) and imaginary (b) part of the normalized space-time correlation functions in (28) and (34).

Similarly, several existing F-to-M correlation functions can be obtained by simplifying the the 3-D MIMO M-to-M space-

time correlation function in (34) or (28). For example, the Clarke's temporal correlation function $J_0(2\pi f_{R\max}\tau)$ [27] can be obtained from (34) using the parameters $k_R = \beta_{R_m} = 0$ (2-D isotropic scattering around $\mathrm{R_x}$), $f_{T\max} = d_T = d_R = 0$ (stationary $\mathrm{T_x}$, single-antenna $\mathrm{T_x}$ and $\mathrm{R_x}$), and no scattering around $\mathrm{T_x}$ (set $k_T = f_{T\max} = d_T = 0$ to cancel one of the Bessel functions). Expressions for other temporal correlation functions based on the one-ring model [20] and based on the one-cylinder model [13], [28] can be similarly obtained using (34) and (28), respectively. Finally, assuming 2-D isotropic scattering, the spatial correlation function for single-input multiple-output (SIMO) F-to-M channels $J_0(2\pi d_R/\lambda)$ [14], can be obtained from (34) with $k_T = k_R = 0$, $\beta_{T_m} = \beta_{R_m} = \psi_R = 0$, $d_T = 0$, and $\tau = 0$. However, generalized expressions for 2-D and 3-D MIMO F-to-M space-time correlation functions cannot be obtained from the 3-D MIMO M-to-M space-time correlation functions in (34) or (28). For example, the 2-D MIMO F-to-M space-time correlation function $\exp(j2\pi d_T\cos\theta_T/\lambda)I_0\left(\sqrt{x_2^2+y_2^2}\right)/I_0(k_R)$ [20], where $x_2 = j2\pi d_R\cos\theta_R/\lambda - j2\pi\tau f_{R\max}\cos\gamma_R + k_R\cos\mu_R$, $y_2 = j2\pi d_T\Delta\sin\theta_T/\lambda + j2\pi d_R\sin\theta_R - j2\pi\tau f_{R\max}\sin\gamma_R + k_R\sin\mu_R$, and $\Delta = R_r/D$, cannot be obtained from (34). Similarly, the 3-D MIMO F-to-M space-time correlation functions in [13], [28] are not special cases of (28). The underlying reason is that the distance traversed by a ray in a double-bounced M-to-M channel is significantly different from the distance traversed by a ray in a single-bounced F-to-M channel, leading to different parameters in the space-time correlation functions. Conversely, the 3-D MIMO M-to-M space-time correlation functions in (34) or (28) are not straightforward extensions of the F-to-M space-time correlation functions in [20], [13], [28].

The 2-D space-time correlation function for M-to-M channels suggests that two vertically placed antennas are completely correlated and no diversity gain is available. However, the 3-D space-time correlation function shows that vertically placed antennas can have small correlations and provide considerable diversity gain. To illustrate this, Fig. 3 shows the spatial correlation functions of two uniformly and vertically spaced antennas at the $\mathrm{T_x}$ for several maximum elevation angles β_{T_m}. Other parameters used to obtain curves in Fig. 3 are $L_R = 1$, $\theta_T = \theta_R = 0$, $\psi_T = \pi/2$, $\psi_R = 0$, $\gamma_T = \gamma_R = 0$, and $k_T = k_R = 0$. As the maximum elevation angle β_{T_m} increases from 1° to 20°, the correlation between the two antennas reduces dramatically.

Finally, Fig. 4 compares the Doppler power spectral density (D-psd) of the complex faded envelope in (5) with the measured SISO narrowband D-psd in [6]. The D-psd is defined as the Fourier transform of space-time correlation function and is calculated as $S_{pq,\tilde{p}\tilde{q}}[f] = \mathcal{F}\{R_{pq,\tilde{p}\tilde{q}}[\tau]\} = \mathcal{F}\left\{R^T_{p,\tilde{p}}[\tau]\right\} \odot \mathcal{F}\left\{R^R_{q,\tilde{q}}[\tau]\right\}$, where $\odot$ denotes convolution. Parameters used to obtain simulation results in Fig. 4 are $L_t = L_r = 1$, $\beta_{Tm} = \beta_{Rm} = 15^\circ$, $\theta_T = \theta_R = \pi/4$, $\psi_T = \psi_R = \pi/3$, $\gamma_T = 0$, $\gamma_R = 10^\circ$, $k_T = k_R = 3.3$, $\mu_T = 0$, $\mu_R = \pi$, and $f_{T\max} = f_{R\max} = 100$ Hz. The measured results are taken from Fig. 7(a) (urban environment) of [6]. The close agreement between the theoretical and empirical curves confirms the utility of the proposed narrowband model.

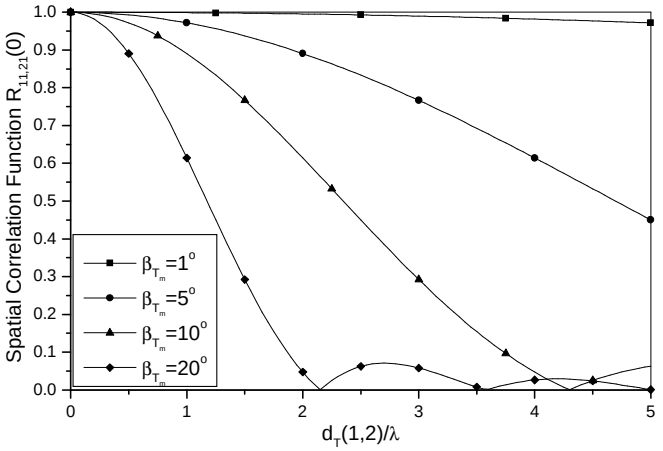

Fig. 3. The normalized spatial correlation functions of two uniformly and vertically spaced antennas at the $\mathrm{T_x}$, for several maximum elevation angles β_{T_m}.

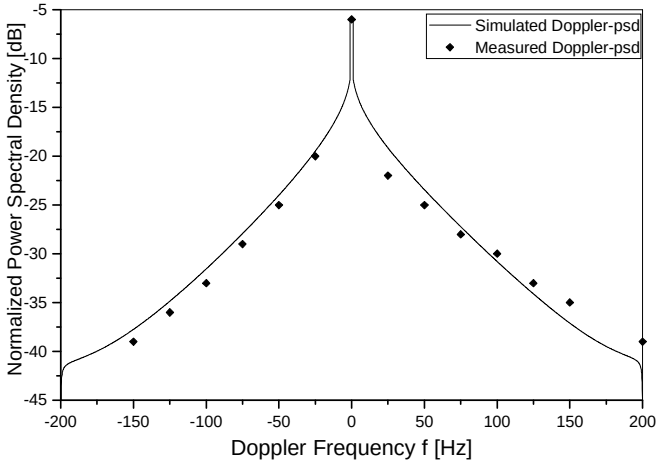

Fig. 4. The normalized simulated and measured [6] Doppler power spectra.

IV. 3-D Simulation Models for MIMO Mobile-to-Mobile Channels

The reference model described in Section II assumes an infinite number of scatterers, which prevents practical implementation. Here, we design simulation models with a finite number of scatterers, while still matching the statistical properties of the reference model.

Using the reference model in (5) with a finite number of scatterers and assuming 3-D non-isotropic scattering, the following function is considered for the received complex faded envelope

$$h_{pq}(t) = \frac{1}{\sqrt{MN}}\sum_{m=1}^{M}\sum_{n=1}^{N} a_{p,m}\; b_{n,q}\; e^{j\phi_{mn}} \times e^{j2\pi t\left[f_{T\max}\cos(\alpha_T^{(m)}-\gamma_T)\cos\beta_T^{(m)} + f_{R\max}\cos(\alpha_R^{(n)}-\gamma_R)\cos\beta_R^{(n)}\right]}, \tag{35}$$

where parameters $a_{p,m}$ and $b_{n,q}$ are defined in (6) and (7). The angles of departure, $\alpha_T^{(m)}$ and $\beta_T^{(m)}$, and the angles of arrival, $\alpha_R^{(n)}$ and $\beta_R^{(n)}$, are random variables and the angles of departure are independent from the angles of arrival. The phases ϕ_{mn} are also random variables uniformly distributed

on the interval $[-\pi, \pi)$ and independent from the angles of departure and angles of arrival. The AAoDs, $\alpha_T^{(m)}$, and the AAoAs, $\alpha_R^{(n)}$, are modeled using the von Mises pdfs $f(\alpha_T) = \exp[k_T \cos(\alpha_T - \mu_T)]/(2\pi I_0(k_T))$ and $f(\alpha_R) = \exp[k_R \cos(\alpha_R - \mu_R)]/(2\pi I_0(k_R))$, respectively. They are generated as follows:

$$\alpha_T^{(m)} = F_T^{-1}(\eta_m), \quad (36)$$

$$\alpha_R^{(n)} = F_R^{-1}(\delta_n), \quad (37)$$

for $m = 1, \ldots, M$, $n = 1, \ldots, N$. Function $F_{T/R}(\ \cdot\ )^{-1}$ denotes the inverse function of the von Mises cumulative distribution function (cdf) and can be evaluated using method in [29]. Parameters η_m and δ_n are independent random variables uniformly distributed on the interval $(0, 1)$. The EAoDs, $\beta_T^{(m)}$, and the EAoAs, $\beta_R^{(n)}$, are modeled using the pdfs $f(\beta_T) = \pi \cos(\pi\beta_T/(2\beta_{T_m}))/(4\beta_{T_m})$ and $f(\beta_R) = \pi \cos(\pi\beta_R/(2\beta_{R_m}))/(4\beta_{R_m})$, respectively, and are generated as follows:

$$\beta_T^{(m)} = \frac{2\beta_{T_m}}{\pi} \arcsin(2\nu_m - 1), \quad (38)$$

$$\beta_R^{(n)} = \frac{2\beta_{R_m}}{\pi} \arcsin(2\zeta_n - 1), \quad (39)$$

for $m = 1, \ldots, M$, $n = 1, \ldots, N$, where ν_m and ζ_n are independent random variables uniformly distributed on the interval $(0, 1)$.

For the maximum elevation angles β_{T_m} and β_{R_m} in the range $0^\circ \leq \beta_{T_m}, \beta_{R_m} \leq 20^\circ$ the elevation angles can be approximated using $\cos\beta_T^{(m)}, \cos\beta_R^{(n)} \approx 1$, $\sin\beta_T^{(m)} \approx \beta_T^{(m)}$, and $\sin\beta_R^{(n)} \approx \beta_R^{(n)}$. Then, the complex faded envelope in (35) can be approximated as

$$h_{pq}(t) \approx \frac{1}{\sqrt{M_A M_E N_A N_E}} \sum_{m,i=1}^{M_A,M_E} \sum_{n,k=1}^{N_A,N_E} c_{p,m,i} d_{n,k,q} \times e^{j2\pi t\left[f_{T\max}\cos(\alpha_T^{(m)}-\gamma_T)+f_{R\max}\cos(\alpha_R^{(n)}-\gamma_R)+j\phi_{m,i,n,k}\right]}, \quad (40)$$

where $M_A M_E = M$, $N_A N_E = N$, parameters $c_{p,m,i}$ and $d_{n,k,q}$ are defined as

$$c_{p,m,i} = e^{-j\frac{2\pi}{\lambda}[\frac{D}{2}+R_t-d_{T_x}^{(p)}\cos\alpha_T^{(m)}-d_{T_y}^{(p)}\sin\alpha_T^{(m)}-d_{T_z}^{(p)}\sin\beta_T^{(i)}]}, \quad (41)$$

$$d_{n,k,q} = e^{-j\frac{2\pi}{\lambda}[\frac{D}{2}+R_r-d_{R_x}^{(q)}\cos\alpha_R^{(n)}-d_{R_y}^{(q)}\sin\alpha_R^{(n)}-d_{R_z}^{(q)}\sin\beta_R^{(k)}]}, \quad (42)$$

and $d_{T_x/R_x}^{(p/q)}$, $d_{T_y/R_y}^{(p/q)}$, and $d_{T_z/R_z}^{(p/q)}$ are defined as in (8) - (13).

A. Deterministic and Statistical 3-D MIMO M-to-M Simulation Models

First, we propose an ergodic statistical (deterministic) model. This model has only the phases $\phi_{m,i,n,k}$ as random variables and needs only one simulation trial to obtain the desired statistical properties. We use the complex faded envelope in (40) and generate the AAoDs, AAoAs, EAoDs, and EAoAs as follows:

$$\alpha_T^{(m)} = F_T^{-1}\left(\frac{m-0.5}{M_A}\right), \quad (43)$$

$$\alpha_R^{(n)} = F_R^{-1}\left(\frac{n-0.5}{N_A}\right), \quad (44)$$

$$\beta_T^{(i)} = \frac{2\beta_{T_m}}{\pi} \arcsin\left(\frac{2i-1}{M_E} - 1\right), \quad (45)$$

$$\beta_R^{(k)} = \frac{2\beta_{R_m}}{\pi} \arcsin\left(\frac{2k-1}{N_E} - 1\right), \quad (46)$$

for $m = 1, \ldots, M_A$, $n = 1, \ldots, N_A$, $i = 1, \ldots, M_E$, $k = 1, \ldots, N_E$, respectively.

For $M, N \to \infty$, our deterministic model can be shown to exhibit properties of the reference model. The space-time correlation function of the complex faded envelope in (40) matches the approximate space-time correlation function in (34). The derivation of the space-time correlation function of the complex faded envelope in (40) is omitted for brevity.

Fig. 5 shows the real part of the space-time correlation function for the deterministic model with $M_A = 30$, $M_E = 5$, $N_A = 30$, and $N_E = 5$ scatterers and a uniform linear antenna array with $L_T = L_R = 2$ antennas. Other parameters used to obtain the curves in Fig. 5 are $d_T = d_R = 1\lambda$, $\theta_T = \theta_R = \pi/3$, $\psi_T = \psi_R = \pi/4$, $\gamma_T = \pi/6$, $\gamma_R = \pi/12$, $\beta_{T_m} = \beta_{R_m} = 15^\circ$, and $k_T = k_R = 0$. Fig. 5 does not show the imaginary part of the space-time correlation function because it is zero for $k_T = k_R = 0$. The results show that the space-time correlation function of the deterministic model closely matches the theoretical one in the range of normalized time delays, $0 \leq f_{T\max} T_s \leq 5$. The deterministic model can match the theoretical one over a wider range of normalized time delays if a larger number of scatterers is used in the simulation model.

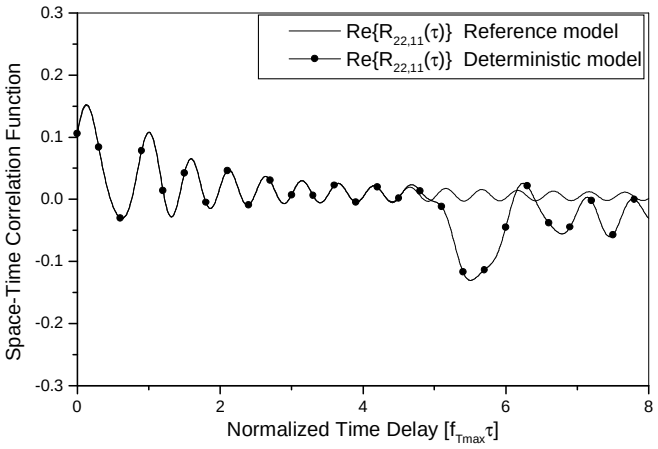

Fig. 5. The real part of the space-time correlation function of the deterministic and reference models.

Deterministic simulators are often used because they are easy to implement and have short simulation times. However, they do not reflect actual channel realizations because their scatterers are placed at specific sights for all simulation trials. By allowing both the phases and Doppler frequencies to be random variables, our deterministic model can be modified to better model the fading processes. Furthermore, this new (statistical) model matches statistical properties of the reference

model over a wider range of normalized time delays, while at the same time requiring a smaller number of scatterers. The statistical properties of the statistical model vary for each simulation trial, but will converge to desired ensemble averaged properties when averaged over a sufficient number of simulation trials.

We use the complex faded envelope in (40) and generate the AAoDs, AAoAs, EAoDs, and EAoAs as follows:

$$\alpha_T^{(m)} = F_T^{-1}\left(\frac{m+\theta_A-1}{M_A}\right), \quad (47)$$

$$\alpha_R^{(n)} = F_R^{-1}\left(\frac{n+\psi_A-1}{N_A}\right), \quad (48)$$

$$\beta_T^{(i)} = \frac{2\beta_{T_m}}{\pi}\arcsin\left(\frac{2(i+\theta_E-1)}{M_E}-1\right), \quad (49)$$

$$\beta_R^{(k)} = \frac{2\beta_{R_m}}{\pi}\arcsin\left(\frac{2(k+\psi_E-1)}{N_E}-1\right), \quad (50)$$

for $m = 1,\ldots,M_A$, $n = 1,\ldots,N_A$, $i = 1,\ldots,M_E$, $k = 1,\ldots,N_E$, respectively. The parameters θ_A, ψ_A, θ_E, and ψ_E are independent random variables uniformly distributed on the interval $[0,1)$.

For arbitrary number of scatterers, i.e., any M, N, our statistical model can be shown to exhibit properties of the reference model. The derivation of the space-time correlation function of the complex faded envelope in (40) is omitted for brevity.

Fig. 6 shows the real part of the space-time correlation function for the statistical model with $M_A = 20$, $M_E = 3$, $N_A = 20$, and $N_E = 3$ scatterers, $N_{\text{stat}} = 50$ simulation trials and an uniform linear antenna array with $L_T = L_R = 2$ antennas. Other parameters are the same as in Fig. 5. The

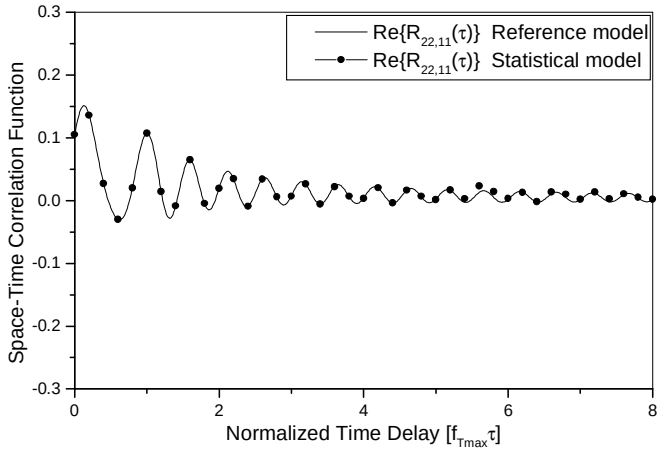

Fig. 6. The real part of the space-time correlation function of the statistical and reference models. The curves are obtained using parameters $d_T = d_R = 1\lambda$, $\theta_T = \theta_R = \pi/3$, $\psi_T = \psi_R = \pi/4$, $\gamma_T = \pi/6$, $\gamma_R = \pi/12$, $\beta_{T_m} = \beta_{R_m} = 15°$, $k_T = k_R = 0$, $L_T = L_R = 2$, $M_A = 20$, $M_E = 3$, $N_A = 20$, and $N_E = 3$ scatterers, and $N_{\text{stat}} = 50$ simulation trials.

results in Figs. 5 and 6 show that the space-time correlation function of the statistical model matches that of the reference model over a wider range of normalized time delays, i.e., $0 \le f_{T\max}T_s \le 10$, compared to the space-time correlation function of the deterministic model.

V. Numerical Analysis of M-to-M Channel Capacity

In this section, we first briefly review the MIMO channel capacity and show that our simulation models can be used to evaluate M-to-M channel capacity. Then, we evaluate the effect of the space-time correlation on the outage capacity of uniform linear antenna arrays. Finally, we compare the capacities of uniform linear, uniform circular, and spherical antenna arrays to determine the best antenna configuration.

A. Review of MIMO Channel Capacity

The instantaneous channel capacity (in bit/s/Hz) of a stochastic MIMO channel, under an average transmit power constraint is [7], [10]

$$C(t) = \log_2 \det\left(\mathbf{I}_{L_R} + \frac{\rho}{L_T}\mathbf{H}(t)\mathbf{H}^H(t)\right), \quad (51)$$

where it is assumed that $L_T \ge L_R$, the transmitter has no channel knowledge, and the receiver has perfect channel knowledge. In (51), $\mathbf{H}(t) = [h_{ij}(t)]_{L_R \times L_T}$ is the $L_R \times L_T$ matrix of complex faded envelopes, $(\ \cdot\ )^H$ denotes the transpose conjugate operation, $\det(\ \cdot\ )$ denotes the matrix determinant, $\mathbf{I}_{L_R}$ is the $L_R \times L_R$ identity matrix, and ρ is the average signal-to-noise ratio (SNR). In this paper, the ergodic capacity of a MIMO channel is defined as the expectation of the instantaneous capacity over time, i.e.,

$$\mathrm{E}[C(t)] = \mathrm{E}\left[\log_2 \det\left(\mathbf{I}_{L_R} + \frac{\rho}{L_T}\mathbf{H}(t)\mathbf{H}^H(t)\right)\right]. \quad (52)$$

In the practice, the outage capacity is often used to characterize the properties of the MIMO channel. Here, the outage capacity C_{out} is associated with an outage probability P_{out} which gives the probability that the instantaneous channel capacity, C, falls below C_{out}.

There are several ways to generate the channel matrix $\mathbf{H}$. One way is to use the simulation models proposed in Section IV. The elements of the channel matrix can be obtained directly, using (40). We will refer to these models as the deterministic and statistical physical models. The other way is to generate the channel matrix as a product of the white channel matrix and the square root of desired correlation matrix. We will refer to this model as the non-physical model. The non-physical model generates the M-to-M channel matrix as [16]

$$\mathbf{H} = (\mathbf{R}_R[0])^{1/2}\mathbf{G}(\mathbf{R}_T[0])^{T/2}, \quad (53)$$

where $\mathbf{G}$ is an $L_R \times L_T$ stochastic matrix with complex Gaussian i.i.d. entries, $(\ \cdot\ )^{1/2}$ denotes the matrix square root operation, $(\ \cdot\ )^T$ denotes the transpose operation, and $\mathbf{R}_R[0]$ and $\mathbf{R}_T[0]$ are the $L_R \times L_R$ receive and $L_T \times L_T$ transmit correlation matrices, respectively. The elements of matrices $\mathbf{R}_R[0]$ and $\mathbf{R}_T[0]$ are obtained using (34).

Here we compare the ergodic capacities obtained using the non-physical and physical models. Fig. 7 shows the ergodic capacity against SNR, ρ, for several uniform linear antenna arrays ($L_T = L_R = 2$, $L_T = L_R = 4$, and $L_T = L_R = 6$). The parameters used to obtain the curves in Fig. 7 are $\theta_T =$

$\theta_R = \pi/4$, $\psi_T = \psi_R = \pi/6$, $\gamma_T = 0$, $\gamma_R = 20°$, $\beta_{T_m} = \beta_{R_m} = 15°$, $k_T = k_R = 5$, $\mu_T = \pi/2$, and $\mu_R = 3\pi/2$. The spacing between two adjacent antenna elements at the $\mathrm{T_x}$ and $\mathrm{R_x}$ is chosen to be 0.5λ. The deterministic simulation model uses $M_A = N_A = 60$, and $M_E = N_E = 5$ scatterers, whereas the statistical simulation model uses $M_A = N_A = 20$, and $M_E = N_E = 3$ scatterers and $N_{\mathrm{stat}} = 50$ simulation trials. Results show good agreement between the non-physical and physical models.

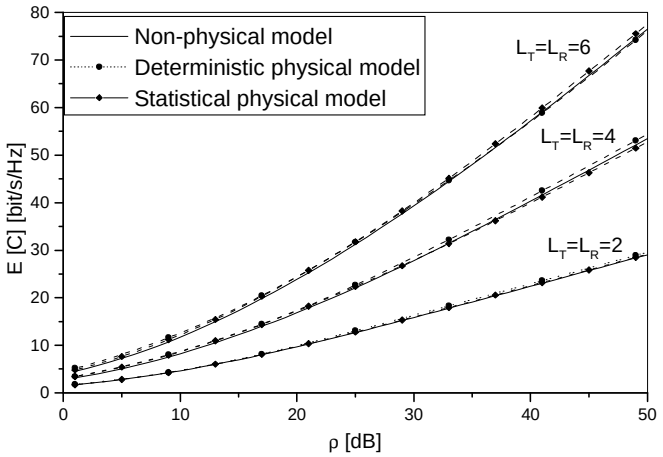

Fig. 7. Comparison of the ergodic capacities obtained using the non-physical model and the deterministic and statistical physical models.

B. Effect of Space-Time Correlation on Outage Capacity of ULAs

In this section, the effect of the space-time correlation on the outage capacity of ULAs is investigated. In all simulations, the outage capacity C_{out} is calculated for a 1% outage probability and the statistical physical model is used to calculate the outage capacity. The coordinates of antenna elements at the $\mathrm{T_x}$ and $\mathrm{R_x}$ are calculated using equations (14) - (16). A normalized sampling period $f_{T\max}T_s = 0.01$ ($f_{T\max} = f_{R\max}$ are the maximum Doppler frequencies and T_s is the sampling period) is used in all simulations. Finally, the statistical physical model uses $M_A = N_A = 20$, and $M_E = N_E = 3$ scatterers and $N_{\mathrm{stat}} = 50$ simulation trials.

Fig. 8 shows the outage capacity as a function of the spacing between the $\mathrm{T_x}$ and $\mathrm{R_x}$ antenna array elements. Parameters used to obtain the curves in Fig. 8 are $\gamma_T = \gamma_R = 20°$, $\theta_T = \theta_R = \pi/4$, $\psi_T = \psi_R = \pi/3$, $\beta_{T_m} = \beta_{R_m} = 15°$, $\rho = 15$ dB, $L_T = L_R = 3$, $\mu_T = 0°$, $\mu_R = 180°$, and $k_T = k_R = 10$ (non-isotropic scattering environment). We can observe that increasing antenna element spacings d_T and d_R from 0.1λ to 2λ increases the capacity from 6 bit/s/Hz to 12 bit/s/Hz. However, increasing antenna element spacings d_T and d_R beyond 2λ has a negligible effect on the capacity. These results differ from results obtained for cellular F-to-M channels (with fixed, elevated base station antennas), where increasing the $\mathrm{R_x}$ antenna element spacing d_R beyond 5λ and the $\mathrm{T_x}$ antenna element spacing d_T beyond 2λ has a negligible effect on the capacity [7].

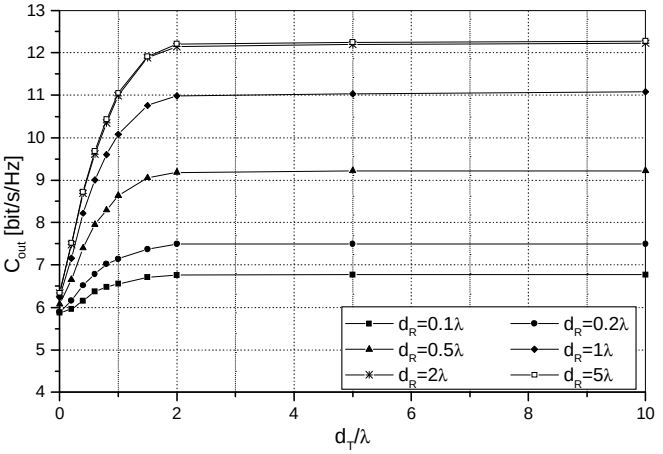

Fig. 8. The outage capacity as a function of spacing between the $\mathrm{T_x}$ and $\mathrm{R_x}$ antenna array elements.

Fig. 9 shows the influence of the $\mathrm{T_x}$ and $\mathrm{R_x}$ antenna array orientations on the capacity when $\mathrm{T_x}$ and $\mathrm{R_x}$ antenna arrays are placed in the x - y plane. To analyze antenna array

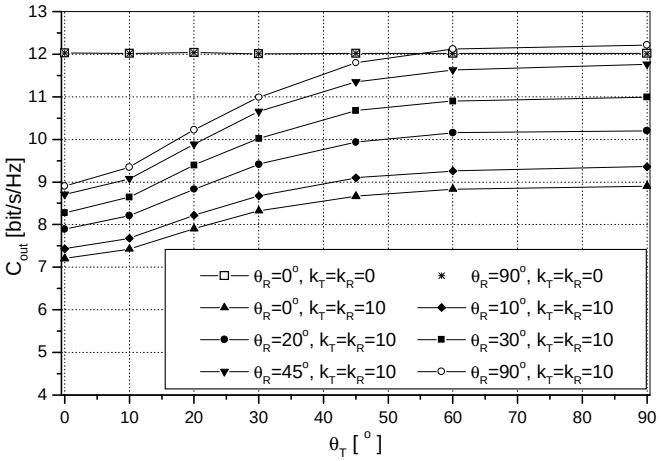

Fig. 9. The outage capacity as a function of the $\mathrm{T_x}$ and $\mathrm{R_x}$ antenna array orientations, θ_T and θ_R.

orientations only in the x - y plane, the elevation angles ψ_T and ψ_R are set to zero. The parameters used to obtain the curves in Fig. 9 are $\gamma_T = \gamma_R = 20°$, $\theta_T = \theta_R = \pi/4$, $d_T = d_R = 1\lambda$, $\rho = 15$ dB, $L_T = L_R = 3$, $\mu_T = 0°$ and $\mu_R = 180°$. From Fig. 9, we can observe that when 2-D isotropic scattering is assumed ($k_T = k_R = 0$), orientations of the $\mathrm{T_x}$ and $\mathrm{R_x}$ antenna arrays have no influence on the capacity. Note that this property of M-to-M channels is in contrast to cellular F-to-M channels (with elevated base station antennas), where $\mathrm{T_x}$ broadside antenna arrays ($\theta_T = 90°$) and $\mathrm{R_x}$ inline antenna arrays ($\theta_R = 0°$) provide higher capacity than $\mathrm{T_x}$ and $\mathrm{R_x}$ broadside antenna arrays [14], [15]. When 2-D non-isotropic scattering is assumed ($k_T = k_R = 10$), we can observe that the outage capacity is the lowest for inline antenna arrays and the highest for broadside antenna arrays. Increasing antenna angles θ_T and θ_R from $0°$ to $45°$ increases capacity by 4.1 bit/s/Hz. However, a further increase of antenna angles θ_T and θ_R from $45°$ to $90°$ increases the outage

capacity by only 0.8 bit/s/Hz. On the other hand, if local scatterers are centered around the y - axis, (i.e., $\mu_T = 90°$ and $\mu_R = 270°$) the outage capacity will be the lowest for broadside antenna arrays and the highest for inline antenna arrays. This implies that the optimum capacity depends on the relative angle between the $\mathrm{T_x}$ antenna array and the local scatterers around the $\mathrm{T_x}$, i.e., $\mu_T - \theta_T$, and on the relative angle between the $\mathrm{R_x}$ antenna array and the local scatterers around the $\mathrm{R_x}$, i.e., $\mu_R - \theta_R$.

Fig. 10 shows the influence of the $\mathrm{T_x}$ and $\mathrm{R_x}$ antenna elevation angles on the outage capacity. The parameters used to obtain the curves in Fig. 10 are $\gamma_T = \gamma_R = 20°$, $\theta_T = \theta_R = \pi/2$, $\beta_{T_m} = \beta_{R_m} = 15°$, $\rho = 15$ dB, $L_T = L_R = 3$, $\mu_T = 0°$ and $\mu_R = 180°$. From Fig. 10, observe that when isotropic scattering in the x - y plane is assumed ($k_T = k_R = 0$) and the distances between antenna array elements are $d_T = d_R = 0.2\lambda$, increasing antenna angles ψ_T and ψ_R from $0°$ to $45°$ has a small influence on the outage capacity. A further increase in the antenna elevation angles drastically decreases the capacity. When the distance between antenna array elements is increased to $d_T = d_R = 1\lambda$, increasing angles ψ_T and ψ_R from $0°$ to $70°$ has a small influence on the outage capacity. Furthermore, when non-isotropic scattering in the x - y plane is assumed ($k_T = k_R = 10$) and the distances between antenna array elements are $d_T = d_R = 1\lambda$, increasing antenna angles ψ_T and ψ_R from $0°$ to $45°$ decreases the outage capacity by only 0.4 bit/s/Hz. A further increase of antenna elevation angles drastically decreases the outage capacity. Fig. 10 implies that if available area in the x - y plane is not sufficient for the antenna array realization, the antenna array can be moderately tilted without significant loss of outage capacity.

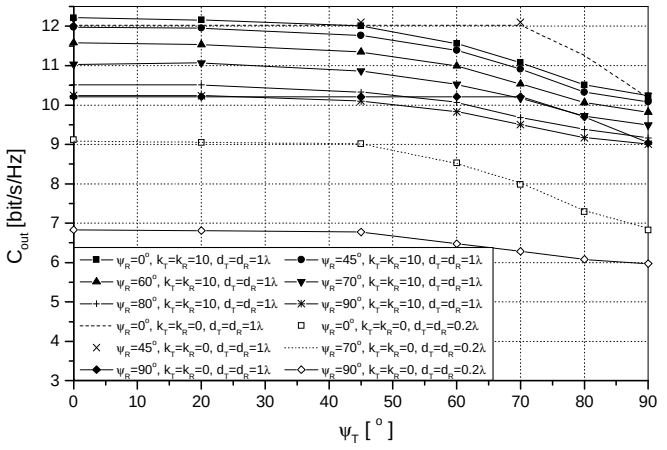

Fig. 10. The outage capacity as a function of the $\mathrm{T_x}$ and $\mathrm{R_x}$ antenna array elevations, ψ_T and ψ_R.

Finally, Fig. 11 shows the capacity as a function of the maximum elevation angles β_{T_m} and β_{R_m}. The parameters used to obtain the curves in Fig. 11 are $\gamma_T = \gamma_R = 20°$, $\theta_T = \theta_R = \pi/4$, $\psi_T = \psi_R = \pi/3$, $d_T = d_R = 1\lambda$, $\rho = 15$ dB, $L_T = L_R = 3$, $\mu_T = 0°$, $\mu_R = 180°$, and $k_T = k_R = 10$. Observe that by increasing maximum elevation angles β_{T_m} and β_{R_m} from $1°$ to $20°$ the outage capacity increases by up to 1 bit/s/Hz. This result implies that the 2-D models actually underestimate available capacity.

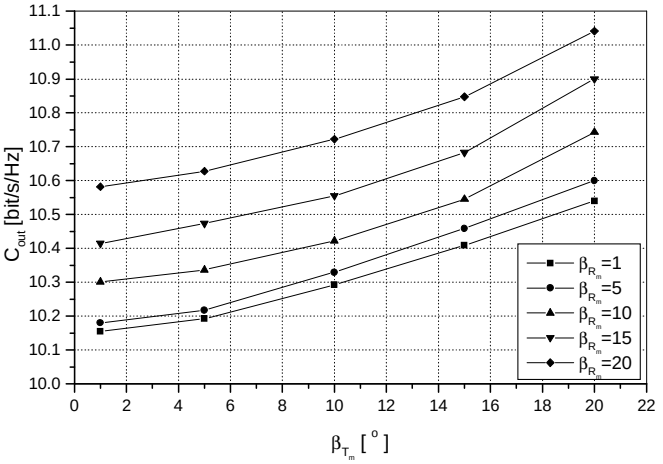

Fig. 11. The outage capacity as a function of the maximum elevation angles β_{T_m} and β_{R_m}.

C. Comparison of Linear, Circular, and Spherical MIMO Antenna Configurations

In the previous section, the effect of the space-time correlation on the outage capacity of ULAs was investigated. Here, we compare the capacities of uniform linear, circular, and spherical antenna arrays. Again, the outage capacity C_{out} is calculated for a 1% outage probability and the physical model is used to calculate the outage capacity. In all simulations, a normalized sampling period $f_{T\max}T_s = 0.01$ is used and $M_A = N_A = 20$, and $M_E = N_E = 3$ scatterers and $N_{\mathrm{stat}} = 50$ simulation trials are used in the statistical simulation model. The angles of motion for the $\mathrm{T_x}$ and $\mathrm{R_x}$ are chosen to be $\gamma_T = \gamma_R = 40°$. The maximum elevation angles are chosen to be $\beta_{T_m} = \beta_{R_m} = 15°$. The number of transmit and receive antennas is set to $L_T = L_R = 8$. Finally, isotropic scattering is assumed in the x - y plane, i.e., $k_T = k_R = 0$.

The coordinates of the ULA elements are calculated as in the previous section. The azimuth and elevation angles used for the ULA are $\theta_T = \theta_R = \pi/4$ and $\psi_T = \psi_R = \arcsin(1/\sqrt{3})$, respectively. The coordinates of the circular antenna array elements at the $\mathrm{T_x}$ and $\mathrm{R_x}$ are calculated using equations (17) - (19). The elevation angles used for the circular antenna arrays are $\psi_T = \psi_R = \arcsin(1/\sqrt{3})$. Finally, the coordinates of the spherical antenna array elements at the $\mathrm{T_x}$ and $\mathrm{R_x}$ are calculated using equations (20) - (22). The azimuth and elevation angles used for the spherical antenna arrays are $\theta_T^{(p)} = 2\pi p/L_T$, $\theta_T^{(\tilde{p})} = 2\pi \tilde{p}/L_T$, $\theta_R^{(q)} = 2\pi q/L_R$, $\theta_R^{(\tilde{q})} = 2\pi \tilde{q}/L_R$, and $\psi_T = \psi_R = \pm\arcsin(1/\sqrt{3})$.

There are two ways to compare antenna arrays. One maintains an equal spacing between two adjacent antenna elements in the uniform linear, circular, and spherical antenna arrays. The other designs uniform linear, circular, and spherical antenna arrays to occupy the same volume.

First, we assume that the spacings between two adjacent antenna elements of the uniform linear, circular, and spherical antenna arrays are equal, i.e., $d_T = d_R = 0.5\lambda$ and $r_T = r_R =$

$0.5\lambda/(2\sin(\pi/8))$. Fig. 12 shows the outage capacity against SNR, ρ, for several uniform linear, circular, and spherical antenna arrays when isotropic scattering is assumed in the x - y plane ($k_T = k_R = 0$). As expected, non-tilted ($\psi_T = \psi_R = 0$) and tilted ($\psi_T = \psi_R = \arcsin(1/\sqrt{3})$) ULAs have a higher outage capacity than non-tilted and tilted circular and spherical antenna arrays because their non-adjacent antenna elements are placed further apart compared to circular and spherical antenna arrays. When isotropic scattering is assumed in the x - y plane, the orientations of ULAs have no influence on the capacity, and hence, ULAs will always provide higher capacity than circular and spherical antenna arrays. Note that when non-isotropic scattering is assumed in the x - y plane ($k_T, k_R > 0$), ULAs have higher capacity than circular and spherical antenna arrays only if the ULA orientation angles θ_T and θ_R are chosen to maximize the relative angles between the $\mathrm{T_x}$ and $\mathrm{R_x}$ antenna arrays and the local scatterers around the $\mathrm{T_x}$ and $\mathrm{R_x}$, i.e., $\mu_T - \theta_T$ and $\mu_R - \theta_R$, respectively. If the angles $\mu_T - \theta_T$ and $\mu_R - \theta_R$ are known to a reasonable accuracy, it is advantageous to deploy uniform linear antenna arrays with optimized angles θ_T and θ_R. Otherwise, circular antenna arrays may be a better choice because they will provide more a consistent outage capacity.

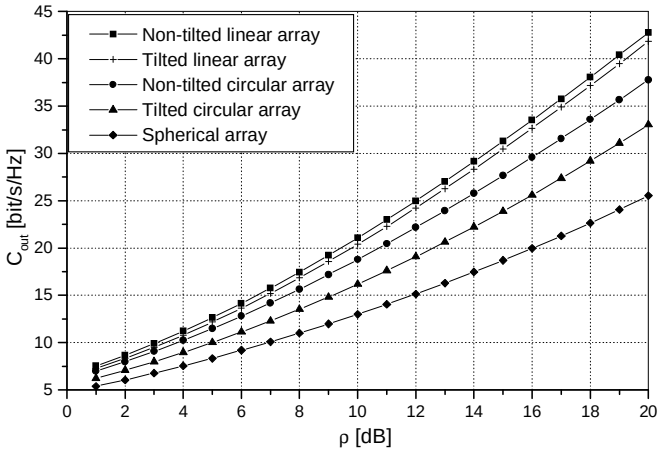

Fig. 12. The outage capacity against SNR, ρ, for several uniform linear, circular, and spherical antenna arrays having equal spacing between two adjacent antenna elements. The curves are obtained using parameters $\gamma_T = \gamma_R = 40^\circ$, $d_T = d_R = 1\lambda$, $L_T = L_R = 8$, and $k_T = k_R = 0$.

In practice, the available volume for antenna array realization and packaging is often constrained. Suppose, for example, that the uniform linear, circular, and spherical antenna arrays are designed to fit in a sphere of radius $(\sqrt{3}/2)\lambda$. Then, the spacing between two adjacent antenna elements of the ULA is $d_T = d_R = (\sqrt{3}/8)\lambda$, whereas the radii of the circular and spherical antenna arrays are $r_T = r_R = (\sqrt{3}/2)\lambda$. It is assumed that omnidirectional antenna elements are realized as patch antennas. Fig. 13 shows the outage capacity against SNR, ρ, for several uniform linear, circular and spherical antenna arrays occupying equal volume. As expected, the tilted ($\psi_T = \psi_R = \arcsin(1/\sqrt{3})$) uniform linear and circular antenna arrays have a smaller outage capacity compared to the non-tilted ($\psi_T = \psi_R = 0$) ones. An interesting result is that non-tilted circular antenna arrays have higher outage capacity than spherical antenna arrays by about 1 $\mathrm{bit/s/Hz}$. Tilted circular and spherical antenna arrays have similar outage capacity, and a much higher outage capacity than non-tilted and tilted ULAs. From Fig. 13 we can conclude that if the available volume for antenna array realization is constrained, circular antenna arrays placed in the x - y plane will provide the highest outage capacity.

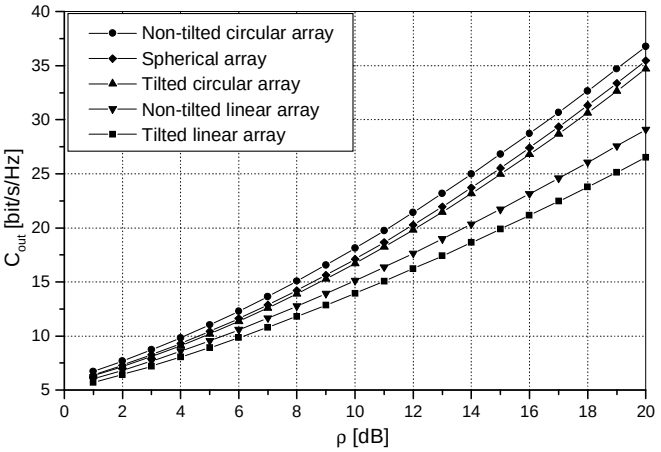

Fig. 13. The outage capacity against SNR, ρ, for several uniform linear, circular and spherical antenna arrays occupying equal volume. The curves are obtained using parameters $\gamma_T = \gamma_R = 40^\circ$, $d_T = d_R = 1\lambda$, $L_T = L_R = 8$, and $k_T = k_R = 0$.

VI. Conclusions

In this paper, the "two-cylinder" geometrical propagation model is introduced. Based on this geometrical model, the 3-D reference model for MIMO M-to-M multipath-fading channels is proposed. From the reference model, the closed-form joint space-time correlation function for a 3-D non-isotropic scattering environment is derived. Furthermore, the deterministic and statistical SoS simulation models for MIMO M-to-M multipath-fading channels are proposed. The statistics of the simulation models are verified by simulation. Finally, these simulation models are used to evaluate the effect of the space-time correlation on the outage capacity of uniform linear antenna arrays and to compare the capacities of linear, circular, and spherical antenna arrays.

References

[1] A. S. Akki and F. Haber, "A statistical model for mobile-to-mobile land communication channel," *IEEE Trans. on Veh. Tech.*, vol. 35, pp. 2–10, February 1986.

[2] A. S. Akki, "Statistical properties of mobile-to-mobile land communication channels," *IEEE Trans. on Veh. Tech.*, vol. 43, pp. 826–831, November 1994.

[3] R. Wang and D. Cox, "Channel modeling for ad hoc mobile wireless networks," *Proc. IEEE VTC'02*, vol. 1, pp. 21–25, Birmingham, AL, May 2002.

[4] C. S. Patel, G. L. Stüber, and T. G. Pratt, "Simulation of Rayleigh-faded mobile-to-mobile communication channels," *IEEE Trans. on Commun.*, vol. 53, pp. 1876–1884, November 2005.

[5] A. G. Zajić and G. L. Stüber, "A new simulation model for mobile-to-mobile Rayleigh fading channels," *Proc. IEEE WCNC'06*, vol. 3, pp. 1266-1270, Las Vegas, NE, April 2006.

[6] J. Maurer, T. Fügen, and W. Wiesbeck, "Narrow-band measurement and analysis of the inter-vehicle transmission channel at 5.2 GHz," *Proc. IEEE VTC'02*, vol. 3, pp. 1274–1278, Birmingham, AL, May 2002.

[7] G. J. Byers and F. Takawira, "Spatially and temporally correlated MIMO channels: Modeling and capacity analysis," *IEEE Trans. on Veh. Tech.*, vol. 53, no. 3, pp. 634–643, May 2004.
[8] M. Pätzold, B. O. Hogstad, N. Youssef, and D. Kim, "A MIMO mobile-to-mobile channel model: Part I-the reference model," *Proc. IEEE PIMRC'05*, vol. 1, pp. 573–578, Berlin, Germany, September 2005.
[9] A. G. Zajić and G. L. Stüber, "Space-Time Correlated MIMO Mobile-to-Mobile Channels," *Proc. IEEE PIMRC'06*, Helsinki, Finland, September 2006.
[10] B. O. Hogstad, M. Pätzold, N. Youssef, and D. Kim, "A MIMO mobile-to-mobile channel model: Part II-the simulation model," *Proc. IEEE PIMRC'05*, vol. 1, pp. 562–567, Berlin, Germany, September 2005.
[11] A.G. Zajić and G.L. Stüber, "Simulation Models for MIMO Mobile-to-Mobile Channels," *Proc. IEEE MILCOM'06*, Washington, D.C., USA, October 2006.
[12] T. Aulin, "A modified model for the fading at a mobile radio channel," *IEEE Trans. on Veh. Tech.*, vol. VT–28, pp. 182–203, 1979.
[13] J. D. Parsons and A. M. D. Turkmani, "Characterisation of mobile radio signals: model description," *IEE Proc. I, Commun., Speach, and Vision*, vol. 138, pp. 549–556, December 1991.
[14] D. Shiu, G. J. Foschini, M. J. Gans, and J. M. Khan, "Fading correlation and its effect on the capacity of multielement antenna systems," *IEEE Trans. on Commun.*, vol. 48, pp. 502–513, March 2000.
[15] P. Almers, F. Tufvesson, P. Karlsson, and A. F. Molisch, "The effect of horizontal array orientation on MIMO channel capacity," *Proc. IEEE VTC'03*, vol. 1, pp. 34–38, April 2003.
[16] D. Gesbert, H. Bölcskei, D. A. Gore, and A. J. Paulraj, "Outdoor MIMO wireless channels: models and performance prediction," *IEEE Trans. on Commun.*, vol. 50, pp. 1926–1934, December 2002.
[17] K. Kalliola, K. Sulonen, H. Laitinen, O. Kivekäs, J. Krogerus, and P. Vainikainen "Angular power distribution and mean effective gain of mobile antenna in different propagation environments," *IEEE Trans. on Veh. Tech.*, vol. 51, pp. 823–838, September 2002.
[18] Y. Yamada, Y. Ebine, and N. Nakajima, "Base station/vehicular antenna design techniques employed in high capacity land mobile communications system," *Rev. Elec. Commun. Lab.*, NTT, pp. 115–121, 1987.
[19] J. Salz and H. Winters, "Effect of fading correlation on adaptive arrays in digital mobile radio," *IEEE Trans. on Veh. Tech.*, vol. 43, pp. 1049–1057, November 1994.
[20] A. Abdi and M. Kaveh, "A space-time correlation model for multielement antenna systems in mobile fading channels," *IEEE Journal on Select. Areas in Commun.*, vol. 20, pp. 550–560, April 2002.
[21] K. I. Pedersen, P. E. Mogensen, and B. H. Fleury, "Power azimuth spectrum in outdoor environments," *IEEE Electronics Letters*, vol. 33, pp. 1583–1584, August 1997.
[22] R. H. Clarke, and W. L. Khoo, "3-D mobile radio channel statistics," *IEEE Trans. on Veh. Tech.*, vol. 46, pp. 798–799, August 1997.
[23] T. Taga, "Analysis for mean effective gain of mobile antennas in land mobile radio environments," *IEEE Trans. on Veh. Tech.*, vol. 39, pp. 117–131, May 1990.
[24] A. Kuchar, J. P. Rossi, and E. Bonek, "Directional macro-cell channel characterization from urban measurements," *IEEE Trans. on Antennas and Prop.*, vol. 48, pp. 137–146, February 2000.
[25] I.S. Gradshteyn and I.M. Ryzhik, *Table of Integrals, Series, and Products* 5^{th} *ed.*. A. Jeffrey, Ed. San Diego CA: Academic, 1994.
[26] H. Kang, G. L. Stüber, T. G. Pratt, and M. A. Ingram, "Studies on the capacity of MIMO systems in mobile-to-mobile environment," *Proc. IEEE WCNC'04*, vol. 1, pp. 363–368, Atlanta, GA, March 2004.
[27] R. H. Clarke, "A statistical theory of mobile-radio reception," *Bell Syst. Tech. J.*, pp. 957–1000, July–Aug. 1968.
[28] S. Y. Leong, Y. R. Zheng, and C. Xiao, "Space-time fading correlation functions of a 3-D MIMO channel model," *Proc. IEEE WCNC'04*, vol. 2, pp. 1127–1132, Atlanta, GA, March 2004.
[29] K. V. Mardia and P. E. Jupp, *Directional Statistics*. New York. Wiley 1999.

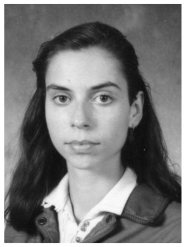

Alenka G. Zajić (S'99) received the B.Sc. and M.Sc. degrees form the School of Electrical Engineering, University of Belgrade, in 2001 and 2003, respectively. From 2001 to 2003, she was a design engineer for Skyworks Solutions Inc., Fremont, CA.

Since 2004, she has been a Graduate Research Assistant with the Wireless Systems Laboratory, and pursuing the Ph.D. degree in the School of Electrical and Computer Engineering, Georgia Institute of Technology. Her research interests are in wireless communications and applied electromagnetic.

Ms. Zajić was recipient of the Dan Noble Fellowship in 2004, awarded by Motorola Inc. and IEEE Vehicular Technology Society for quality impact in the area of vehicular technology.

Gordon L. Stüber (S'81-M'82-SM'96-F'99) received the B.A.Sc. and Ph.D. degrees in Electrical Engineering from the University of Waterloo, Ontario, Canada, in 1982 and 1986 respectively. In 1986, he joined the School of Electrical and Computer Engineering, Georgia Institute of Technology, where is the Joseph M. Pettit Chair Professor.

Dr. Stüber was co-recipient of the IEEE Vehicular Technology Society Jack Neubauer Memorial Award in 1997 for the best systems paper. He became an IEEE Fellow in 1999 for contributions to mobile radio and spread spectrum communications. He received the IEEE Vehicular Technology Society James R. Evans Avant Garde Award in 2003 for contributions to theoretical research in wireless communications.

Dr. Stüber served as General Chair and Program Chair for several conferences, including VTC'96, ICC'98, MMT"00, CTW'02, and WPMC'02. He is a past Editor for IEEE Transactions on Communications (1993-1998), and served on the IEEE Communications Society Awards Committee (1999-2002). He an elected member of the IEEE Vehicular Technology Society Board of Governors (2001-2003, 2004-2006) and received the Outstanding Service Award from the IEEE Vehicular Technology Society.